Supplementary information for Monodisperse PbS Nanocrystals Following Persistent Nucleation and Size Dependent Growth

Benjamin Abécassis*[1], Matthew W. Greenberg[2], Vivekananda Bal[3], Brandon M. McMurtry[2], Michael P. Campos[2], Lilian Guillemeney[1], Benoit Mahler[4], Sylvain Prevost[5,6], Lewis Sharpnack[5], Mark P. Hendricks[2], Daniel De Rosha[2], Ellie Bennett[2], Natalie Saenz[2], Baron Peters*[3], and Jonathan S. Owen*[2]

[1]ENSL, CNRS, Laboratoire de Chimie UMR 5182, 46 allée d'Italie, 69364 Lyon France
[2]Department of Chemistry, Columbia University, New York, New York 10027, United States
[3]Department of Chemical Engineering, University of Illinois, Urbana-Champaign, Illinois 10027, United States
[4]Univ. Lyon, Univ Lyon 1, CNRS, Institu Lumière Matière, F-69622, Villeurbanne, France
[5]ESRF - The European Synchrotron, 71 Avenue des Martyrs, CS 40220, 38043 Grenoble Cedex 9, France
[6]Institut Max von Laue - Paul Langevin (ILL), 71 Avenue des Martyrs, CS 20156, 38042 Grenoble Cedex 9, France

1 Summary table of experimental conditions

sequence number	Thiourea	Temperature (°C)	Recirculation	Reaction volume (mL)
3	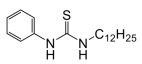	110	Yes	20
6	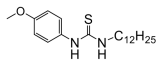	110	Yes	20
7	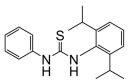	110	Yes	20
8	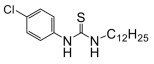	110	Yes	20
13	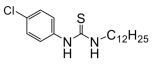	110	No	150
14	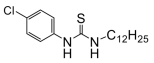	95	No	200
15	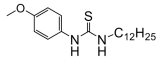	95	No	200

2 Experimental and data fitting Methods

2.1 Chemicals

All manipulations were conducted using standard air-free techniques unless otherwise specified. Origin of the chemicals. Preparation of the thiourea and lead oleate were performed as explained in[1]. Tetradecane is distilled over sodium and stored over molecular sieves

2.2 NMR Kinetics of Thiourea Decomposition

2.2.1 Experimental methods

Synthesis of ^{13}C thioureas: ^{13}C Labeled N-phenyl-N'-dodecylthiourea and N-(4-MeO)phenyl-N'-dodecylthiourea was prepared according to Hendricks et al.[1] by ^{13}C enriched phenyl isothiocyanate prepared from $^{13}CS_2$ (97-99%) by the procedure of Wong[2]. N-(4-Cl)phenyl-N'-dodecylthiourea was prepared using the procedure of Ramadas[3] from the symmetrical thiourea prepared from $^{13}CS_2$ and 4-chloro-aniline.

PbS nanocrystal synthesis: A three-neck round-bottom flask is loaded with lead(II) oleate (166 mg, 0.22 mmol) and hexadecane (14.630 g, 19.0 mL, 64.62 mmol). A thiourea with a ^{13}C labeled thiocarbonyl (0.18 mmol) and diglyme (937 mg, 1.0 mL, 6.98 mmol) are loaded into a 4 mL vial. Both vessels are transferred to a Schlenk line and placed under argon. The three-neck round-bottom flask is brought to 110 °C and the 4 mL vial is brought to 60 °C. Upon reaching the desired reaction temperature the thiourea is quickly injected into the solution of lead(II) oleate and allowed to react for the appropriate amount of time. Quantitative aliquots are taken sequentially throughout the course of the reaction for analysis by ^{13}C NMR and UV-Vis-NIR spectroscopy.

NMR measurements: Aliquots (0.3 mL) for ^{13}C NMR and UV-Vis-NIR absorption spectroscopy measurements are injected into a pre-weighed NMR tube in air and placed into a dry ice acetone bath to prevent further precursor conversion. Immediately prior to collecting an NMR measurement the aliquots are diluted with a known mass of toluene-d_8 (0.25 mL). ^{13}C NMR spectra are collected using an inverse-gated pulse program with extended delay times (10 s) and an Ernst angle of 15° to improve the accuracy of relative peak integrations. The aliquot is subsequently diluted with a known amount of tetrachloroethylene (3 mL) for analysis by UV-Vis-NIR spectroscopy. The thiourea precursor concentration is determined by calculating the fraction of thiourea among the relevant carbonyl resonances (thiourea $\delta = 181$ ppm, N-oleylurea ($\delta = 154$ ppm) and carboiimide ($\delta = 135$ ppm)) and assuming quantitative addition of the thiourea. An automated baseline fitting is applied to each spectrum prior to the collection of integration values. The kinetics of precursor conversion is determined by fitting the temporal evolution of the thiourea concentration to a single exponential decay [precursor](t)=[thiourea](t=0)exp$(-k_r t)$ where [thiourea](t=0) is the initial thiourea concentration, k_r is the rate constant of precursor decomposition, and t is time.

2.2.2 Error Analysis of Solute Concentration

To better understand the uncertainty in $[PbS]_{solute}$ we analyzed several possible sources of error in the ^{13}C NMR measurements used to determine k_{obs}^{NMR}. We determined four possible sources of significant error: (1) conversion of thiourea to PbS during the NMR measurement; (2) solubility of the starting thiourea, the carbodiimide intermediate, and the N-acylurea byproduct; (3) parameters of the pulse program giving non-quantitative results; and (4) decomposition of the N-acyl-urea byproduct lowering the accuracy of $[C{=}E]_{total}$. To test whether there is a significant amount of conversion of the thiourea at room temperature under NMR measurement conditions, we loaded an NMR tube with the contents of a scaled down PbS reaction mixture (300 μL total volume) and diluted it with toluene-d_8 (250 μL). Over the span of >24 hours we observe little change in the overall intensity of the thiocarbonyl and other characteristic resonances (Figure S1). Moreover, we do not see the appearance of either the carbodiimide intermediate or the corresponding N-acylurea. We conclude conversion of thiourea at room temperature is negligible source of uncertainty.

We noticed fairly significant differences ($\simeq$10%) in the extracted value of k_{obs}^{NMR} depending on the deuterated solvent selected for NMR analysis (Figure S2). Here, we see that NMR measurements taken with toluene-d_8 as the solvent give smaller k_{obs}^{NMR} for all conditions reported herein. We hypothesize this can be attributed to the thiourea, carbodiimide, and N-acylurea being more soluble in toluene-d_8 compared to C_6D_6. Qualitatively this can be observed by the appearance of a resonance assigned to the carbodiimide in the toluene-d_8 measurements but not in those using C_6D_6. At early times, when the precursor concentration is high, the solubility issues should be most pronounced. Should [precursor] be incorrectly low, the fitted value of $[\text{thiourea}]_0$ will also be incorrectly low, causing k_{obs}^{NMR} to be artificially large. We conclude the usage of a better solubilizing solvent in necessary to obtain accurate k_{obs}^{NMR} values, therefore toluene-d_8 is used throughout this study.

Collection of quantitative NMR spectra requires sufficiently long delay times (5T1) such that all nuclei of interest have relaxed to their equilibrium ground state. To approximate the necessary delay time to collect quantitative ^{13}C NMR spectra for the experiments herein, we determined the T1 time of N-4-methoxy-phenyl-N'-dodecylthiourea (Figure S3). Here, we measured a T1 time of 10.8 s. In light of this, we suspect there is inherent error in our measurement of [precursor] due to the 10 s delay times used during the collection of NMR spectra. However, we expect this error to be systematic and therefore will not change the trend we observe in k_{obs}^{NMR} between precursor.

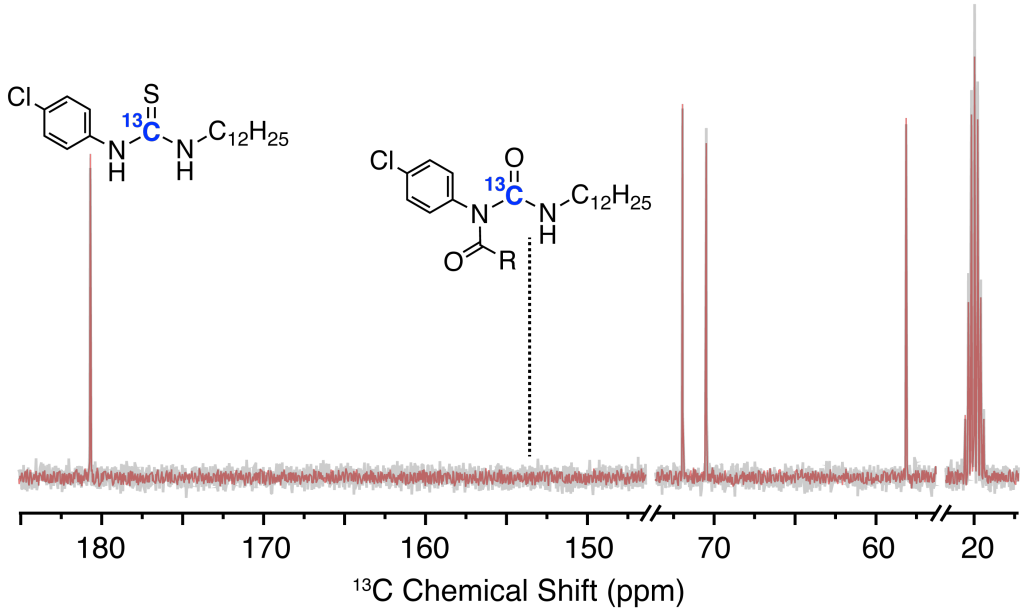

Figure S1. ^{13}C NMR spectra of Pb(oleate)$_2$ and N-4-chloro-phenyl-N'-dodecylthiourea in a mixture of hexadecane, diphenylether, and toluene-d$_8$ measured at 4 hours after mixing (red) and 24 hours after mixing (grey).

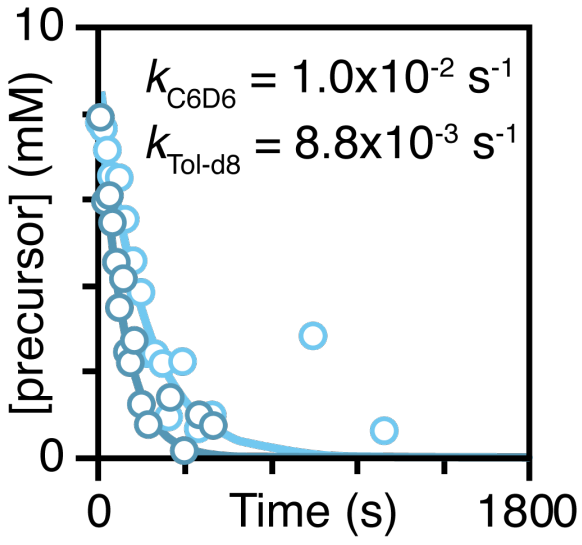

Figure S2. Measurement of [precursor] using ^{13}C NMR spectroscopy for the reaction of N-phenyl-N'-dodecylthiourea and Pb(oleate)$_2$ with C_6D_6 (light blue) or toluene-d$_8$ (dark blue) as the deuterated solvent.

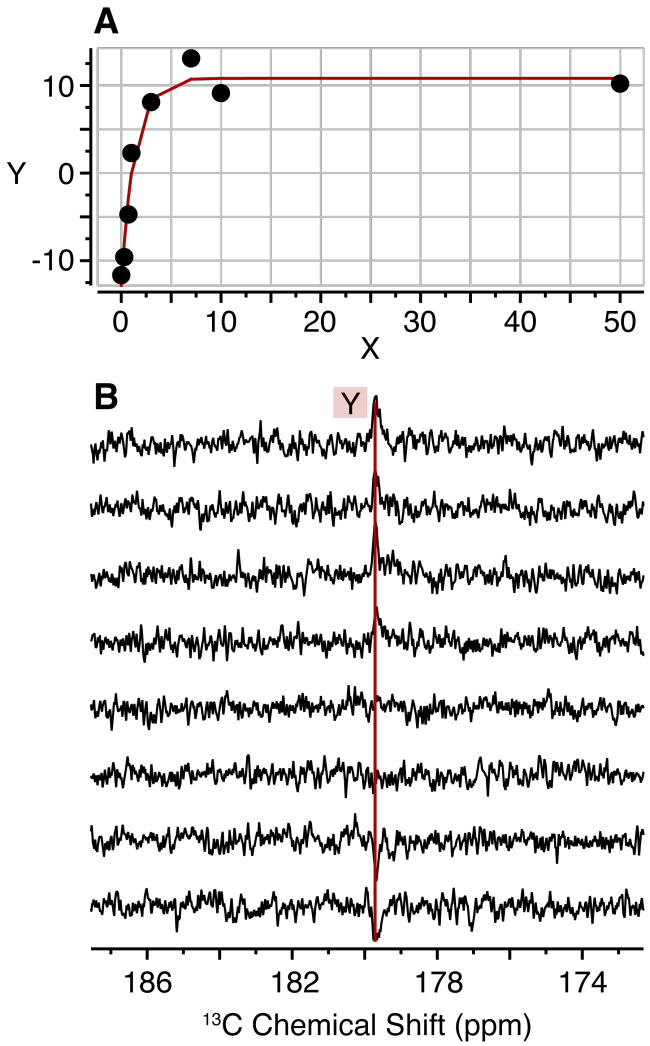

Figure S3. (A) Fitting to determine the T1 value of N-4-methoxy-phenyl-N'-dodecylthiourea using (B) an inversion recovery pulse sequence across a range of τ values.

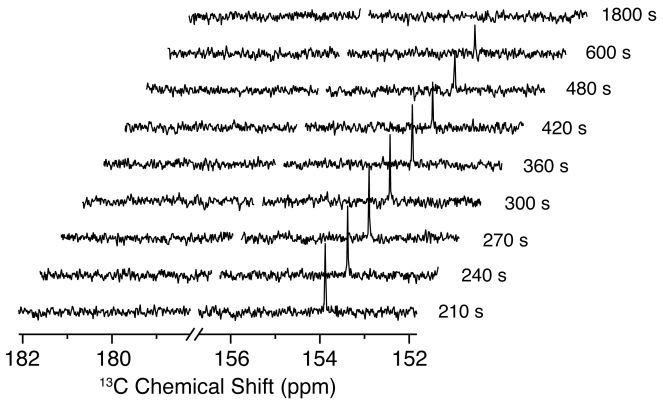

Figure S4. Disappearance of the N-acyl-urea resonance at longer reaction times for the NMR data presented in Figure 3.

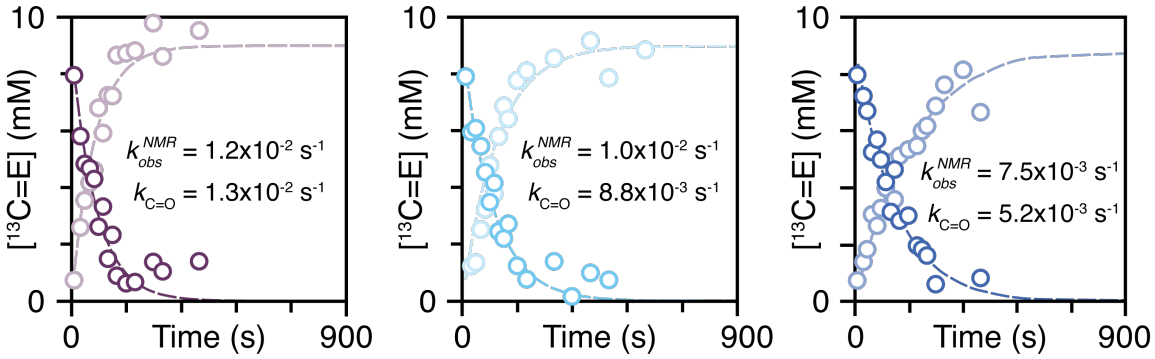

Figure S5. Temporal evolution of the disappearance of precursor (light dots) and appearance of N-acylurea (dark dots) along with their representative exponentials fittings (lines) for PbS reactions from N-4-chloro-phenyl-N'-dodecylthiourea (purple), N-phenyl-N'-dodecylthiourea (light blue), and N-4-methoxy-N'-phenyl-dodecylthiourea (dark blue).

Interestingly, at times later in the reaction (Figure S4), the amount of N-acylurea observed decreases (sometimes to concentrations below the NMR limit). The decomposition pathway of the N-acylurea byproduct in nanocrystal syntheses from thioureas has been previously reported. While the late time disappearance of N-acylurea does not complicate the determination of k_{obs}^{NMR}, the lack of clarity about its rate of decomposition adds more uncertainty to our measurement of k_{obs}^{NMR}. However, independent determination of k-values for the disappearance of precursor (k_{obs}^{NMR}) and appearance N-acylurea (kC=O) give similar values (Figure S5). From this, we conclude that the disappearance of N-acylurea at longer reaction times does not significantly impact our determination of k_{obs}^{NMR}.

2.3 Time-resolved *in situ* SAXS/WAXS experiments

The SAXS/WAXS experiments were performed on the ID02 beamline[4] of the ESRF (European Synchrotron Radiation Facility). The experimental set-up is shown on figure S6. The three-neck round bottom flask contains initially 19 mL of a 9 mM solution lead oleate in hexadecane. The flask is equipped with a thermometer and a UV-VIS probe on the top neck. The fluid is pumped and re-injected through a septum plugged in the last neck of the flask by a peristaltic pump (drive 5201 from Heidolph with a SP Quick head). All the experiments are performed under argon and care is taken to purge all the circuit before each experimental sequence. An oil bath is used to set the temperature. The connection between the needles plunging in the liquid and the X-ray capillary is made with MASTERFLEX Viton tube FDA LS Size 14 with an inner diameter of 1.6 mm. The flow rate within the fluidic circuit is 24.5 mL/min and around 2m of tube are used which correspond to around 4 mL circulating outside the flask during the reaction.

Before injection, a thermal equilibriation time of 10 minutes is respected after the pump is set on. During the course of the reaction, the temperature inside the reacting fluid is monitored and recorded. 1 mL of the thiourea solution in tetraglyme is sampled in a plastic syringe which is then set on a stand. The injection of this solution is controlled remotely from outside the beam-line hutch with a pneumatic piston to which a TTL signal is sent. This time defines the t=0 s of the sequence. At this point SAXS/WAXS acquisitions are triggered. In a typical sequence, 1200 SAXS and WAXS patterns with a duration of 0.3 s are taken every second (i.e. there is a 0.7 s waiting time between two acquisition). A decrease of a few degrees is observed after the thiourea injection but the temperature quickly reaches back the set value.After each sequence, the whole pumping circuit is purged and clean octadecene is circulated. Dilute aqua regia is injected in the capillary and let there for 5 minutes and the signal of the clean capillary is recovered.

To check that the recirculation and exposure to the beam do not affect the reaction, we performed control scaled experiments in which the total volume is multiplied by 10 (200 mL of solvent). In this case, the liquid is not re-injected in the reaction flask after exposure to the X-ray beam but is discarded instead. The volume of the reaction thus decreases with time. We did not observe any difference between the closed and open circulation set-up.

2.4 SAXS/WAXS Data normalization, solvent and capillary signal subtraction

The experiment was performed at an energy of 11.5 keV (wavelength of 1.08 Å). The sample to SAXS detector distance was 1.29707 m which yields a q-range of 0.067 to 5.33 nm^{-1}. After the acquisition, beamline specific corrections were applied to the SAXS and WAXS images and the intensity were radially averaged to yield intensity as a function of wavevector

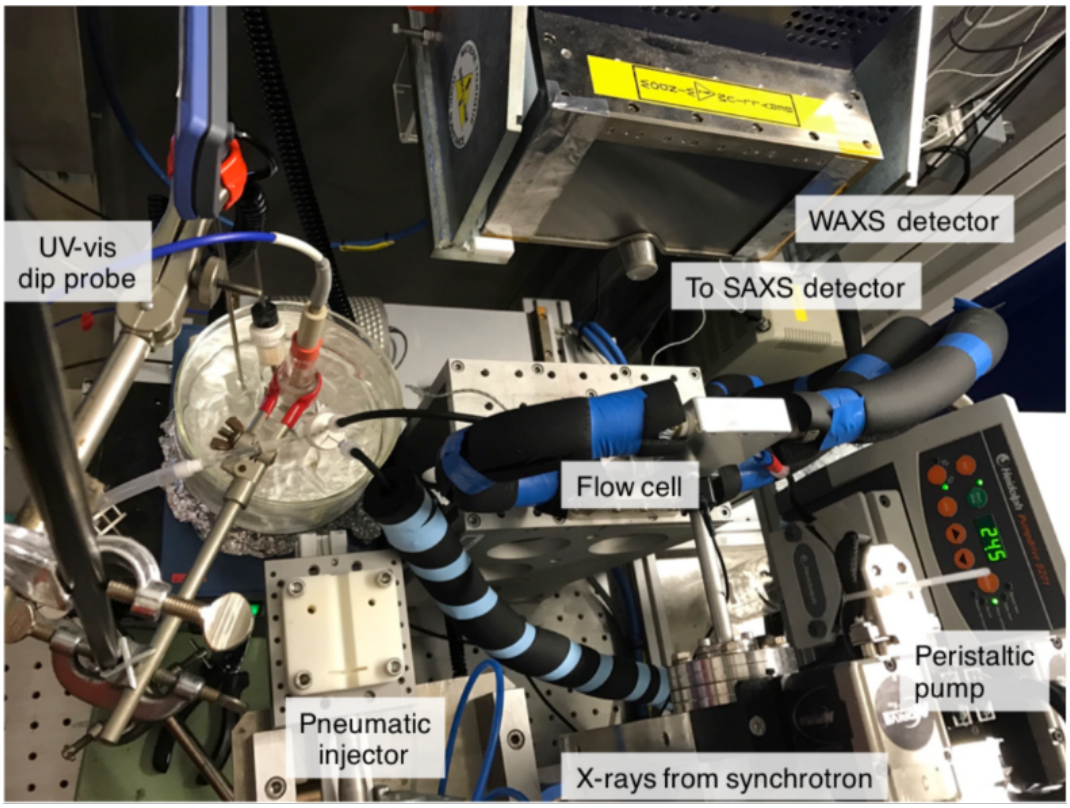

Figure S6. Experimental set-up at the ID02 beamline showing the reaction falsk equiped with the UV-VIS probe. The peristaltic pump extract fluid from the flask, flow it through the flow cell and re-injects it in the flask. X-rays are coming from the bottom of the image and the WAXS detector as well as the entrance to the vaccuum tube containing the SAXS detector are visible on the top.

$q = 4\pi/\lambda \sin(\frac{\theta}{2})$ where θ is the scattering angle. The size of the capillary was determined by scanning it with the X-ray beam before the start of the experiment. All the data normalization and the radial average is performed on the fly on the beamline. The final intensity is divided by the thickness to yield the scattering signal in absolute units (mm^{-1}). Before each experiment at a given temperature, tetradecane is flowed through the capillary at the same temperature and SAXS patterns are acquired at the same acquisition time than during the sequence. This background is then subtracted to all the patterns of the kinetic sequence. Since the X-ray beam hits the capillary exactly at the same place for background acquisition and during the kinetic sequence, we just have to subtract this background in order to subtract the solvent and capillary signals at the same time.

2.5 Data handling and treatment

Starting from the intensity versus wavevector files, all data handling was performed using Ipython[5] and Ipython Notebooks. The non-linear fits were performed using using the Levenberg-Marquardt algorithm implemented in the LMFIT module in Python.

2.6 Fit of the SAXS signal during the sequence

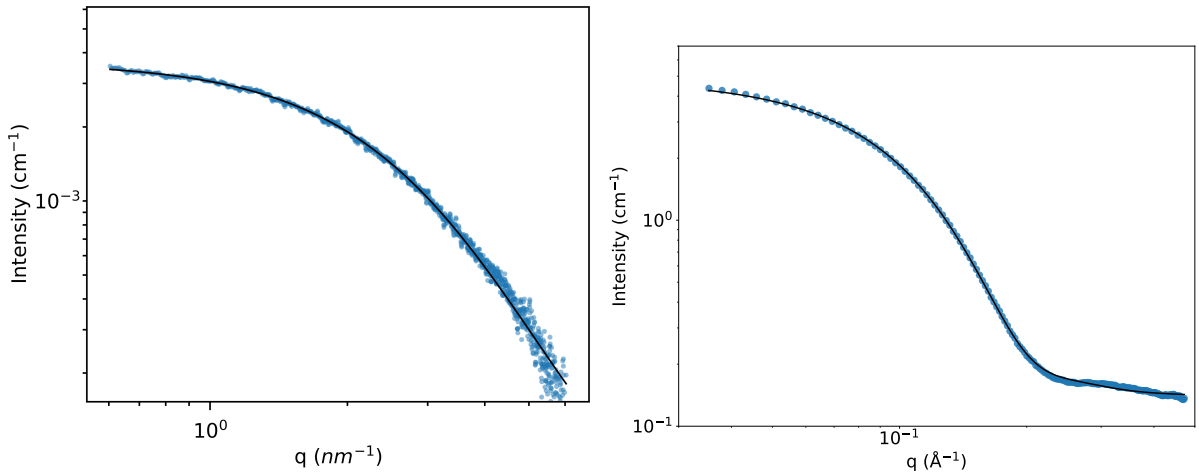

Figure S7. Small angle scattering of lead oleate precursor in tetradecane and corresponding fits to Left: Small angle neutron scattering for a lead oleate solution in deuterated tetradecane.

After the onset of nanoparticle formation the signal is fitted by:

$$I(q,t) = I_0^{NP}(t) \times P_s\left(q, R_{av}^{NP}(t), Z^{NP}(t)\right) + I_0^{p}(t) \times P_s\left(q, R_{av}^{p}, Z^{p}\right) \quad (1)$$

where superscript NP designates the parameters for the nanoparticles and p for the precursors. There are 4 unknown parameters: I_0^{NP}, R_{av}^{NP}, Z^{NP} and I_0^{p}. The signal of the precursor is fitted to a model of spheres with a mean radius of 0.13 nm (figure S7). We also probed the structure of lead oleate dispersed in deuterated tetradecan at the same concentration and temperature using small angle neutron scattering (figure S7). The data were acquired on the D33 beamline at the Institut Laue Langevin[6] and fitted the experimental SANS data to a model of polydispers spheres with a mean radius of 1.74 nm and a polydisersity of 20%. This is consistent with small lead oleate micelles present in solution before the onset of nanoparticle formation. As the reaction proceeds this precursor signal will decrease since lead originally present in these micelles will be incorporated in the nanoparticles. Thus, the signal of the precursor is expected to decrease. This is confirmed by the fact that the SAXS intensity at high q decreases with time and is lower at the end of the reaction than at the begining. We thus impose $I_0^{p}(t=0)$ as an upper bound to the determination of $I_0^{p}(t)$.

We start the fitting procedure by the last SAXS pattern of the sequence and pass the values of the parameters found for the fit at instant t as initial guesses for the fit at instant $t-1$. Starting at the end is justified by the fact that the signal to noise ratio is the highest at this point and also because the large oscillations present ensure a precise determination of the polydispersity at this point. We limit the q-range of the fit to wave vectors comprised between 0.6 and 6 nm^{-1} in order to part of the pattern where the discriminating features for the fit are present i.e. the Guinier regime when the intensity decreases and the oscillation at higher q. By doing so we avoid over-fitting of the low q part at the expense of the more meaningfull part of the SAXS pattern.

Fit examples are shown in the main part of the article. The fits are of excellent quality throughout the sequence with no systematic discrepancy between the experimental data and the model. The oscillations in the late stages of the nanoparticle

formation are very well reproduced by the model.
Finally, it is important to notice that the I_0^p parameter is decreasing during all the course of the reaction. This is consistent with a decrease in the concentration of precursors during the nanoparticle.

To model the SAXS intensity during the formation of the nanoparticles, we use a Schultz distribution of homogeneous spheres:

$$f_s(R) = \left(\frac{Z+1}{R_0}\right)^{Z+1} R^Z \exp\left[-\left(\frac{Z+1}{R_0}\right)R\right] / \Gamma(Z+1) \tag{2}$$

with R_0 the average radius of the spheres and Z the parameter describing the polydispersity of the distribution. Γ is the gamma function. We have shown that the precise shape of the size distribution is difficult to assess when the two first moments of the distribution are equal.[7] This monomodal distribution has several advantages.[8,9] Analytical expressions are available for the small angle scattering of homogeneous spheres with sizes obeying this distribution. Also, its value is 0 for R=0. Finally, all the moments of the distribution can be easily calculated from the three distribution parameters. The root mean square deviation to the mean is given by $\sigma = \frac{R_0}{(Z+1)^{1/2}}$. The N^{th} moment of the size distribution is given by:

$$\langle R^N \rangle = \frac{R_0^N}{(Z+1)^N} \frac{(Z+N)!}{Z!} \tag{3}$$

The intensity scattered by a distribution of non-interaction homogeneous spheres following the Schultz distribution is given by:

$$I(q,R_0,Z) = n\Delta\rho^2 \langle V^2 \rangle P_s(q,R,Z) \tag{4}$$

Where n is the number density of nanoparticle, $\Delta\rho$ is the scattering length density contrast between the nanoparticle and the solvent, V is the volume of the particles and $P_s(q,R,Z)$ is a normalized form factor which tends to 1 when $q \to 0$:

$$P(q) = \frac{\gamma}{(qR_0)^6} \times (1 + (Z+1)(Z+2)(\alpha^{-2} + \varepsilon\cos((Z+3)\beta)/(\alpha^2+4)) - \varepsilon\cos((Z+1)\beta) + \tag{5}$$

$$2(Z+1)\sin((Z+2)\beta)/\sqrt{\alpha^2+4}) \tag{6}$$

With:

$$\alpha = \frac{Z+1}{qR_0}, \tag{7}$$

$$\beta = \arctan(2/\alpha), \tag{8}$$

$$\varepsilon = \left(1 - \frac{4}{\alpha^2+4}\right)^{(Z+1)/2} \tag{9}$$

$$\gamma = \frac{(Z+1)^5}{(Z+2)(Z+3)(Z+4)(Z+5)(Z+6)} \tag{10}$$

Fitting directly expression 4 with unknown parameters n, R_0 and Z yields unreliable results since these parameters are highly coupled. For example, $I(q \to 0)$ depends on three parameters (Z, R and n). Hence, for each SAXS diagram, the minimization algorithm converges towards a local minimum in the parameter space which is not related to previous data. This yields large variations in the fit solutions which are not physical and are just fitting artifacts. In order to circumvent this difficulty, we fit the experimental SAXS diagrams to $I_0 \times P(q,R_0,Z)$ with unknown parameters I_0, R_0 and Z.

From I_0^{NP}, we can extract the concentration in nanoparticle:

$$n^{NP}(t) = \frac{I_0^{NP}}{\Delta\rho^2 \langle V^2 \rangle} \tag{11}$$

We note that $\langle V^2 \rangle = \frac{16\pi^2 R_0^6}{9\gamma} = \langle V \rangle^2 / \gamma$.

2.7 Scattering length density

Scattering length density were obtained from the NIST website [1] We neglected the thermal expansion of the solvent due to temperature and calculated the following values: 7.510×10^{-6} Å^{-2} for tetradecan and 49.973×10^{-6} Å^{-2}. for PbS.

[1] http://www.ncnr.nist.gov/resources/activation/

2.8 WAXS

WAXS patterns are divided in several wave-vector ranges corresponding to different reflections and the intensity is fitted to a gaussian peak model with a linear background. The fitting routine yields σ which is related to the full width at half maximum $\Delta q = 2\sigma\sqrt{(2\ln 2)}$. This value yields the mean crystallite radius through $R = \frac{6.96}{2\Delta q}$ via the Scherrer formula.[10] The position of the maximum q_0 is linked to the lattice expansion E via $E = (q_0 - q_{bulk})/q_0$ where q_{bulk} is the position of the peak in the bulk material. The area under the peak is linked to the volume fraction of cristalline material in the sample. Figure S8 shows the fitting results for the [022] peak. Similar results have been obtained with the other peaks.

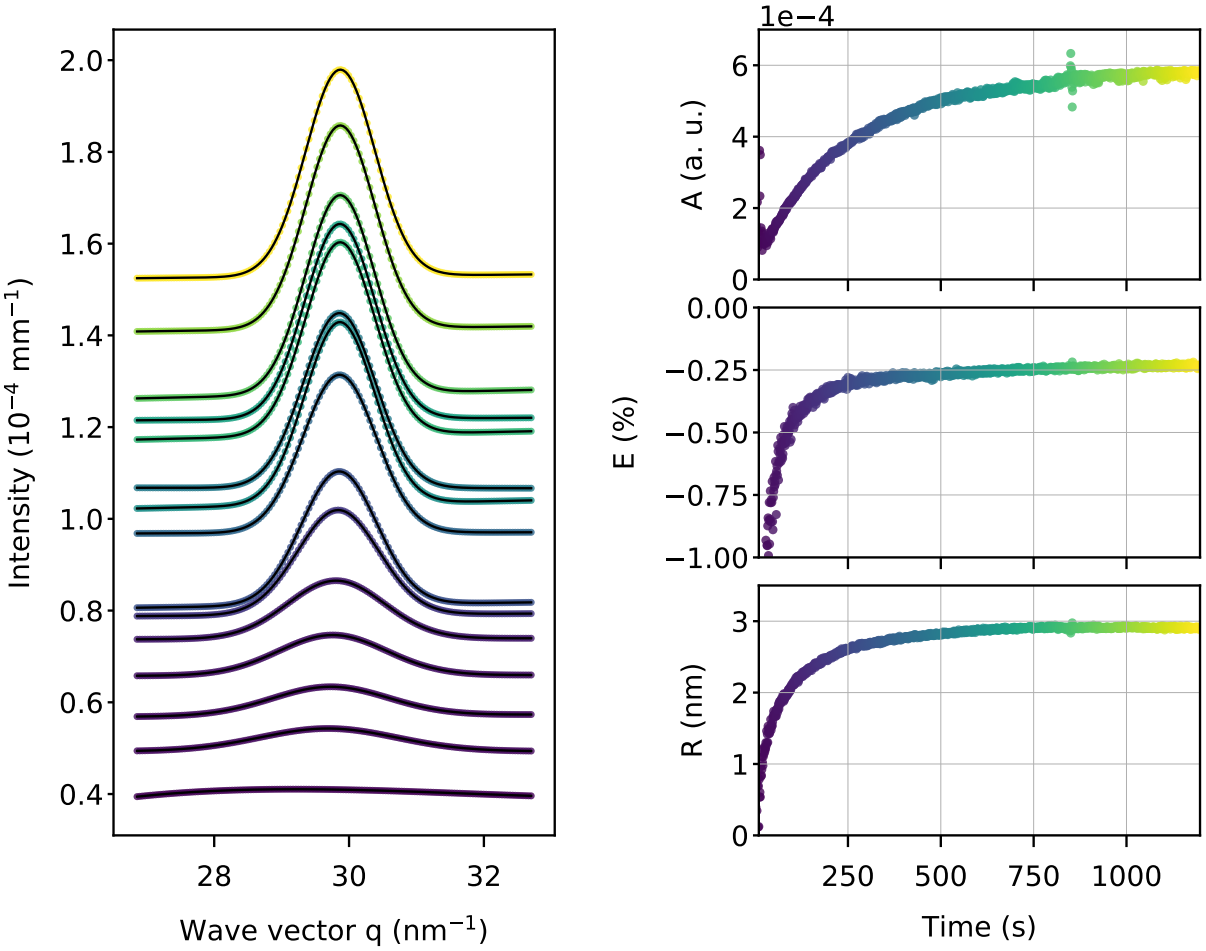

Figure S8. Fits of the [022] diffraction peak with a gaussian lineshape. The left column show fits at different times during the reaction. The right colum displays (from top to bottom) the area under the peak, the strain and radius calculated with the Scherrer formula from the FWHM of the diffraction peak.

2.9 Supplementary discussion on SAXS fitting

In the following we discuss in more depth the fitting of the SAXS pattern and the relevance of the different hypotheses. An important question is whether our SAXS modeling approach could provoke artifacts and yield evolutions in the number of particles or other parameters of the size distribution which do not represent the reality. We applied the principle of model frugality by choosing a model with a minimum number of adjustable parameters that best describes our experimental data. Since the fits of the SAXS data are excellent for all the cases studied with our model, we expect that increasing its complexity and introducing supplementary fitting parameters will not yield a better description of our data. However, in the following, we question the different assumptions we made to see if they are realistic and if they match with prior knowledge on the PbS nanoparticles obtained by other techniques.

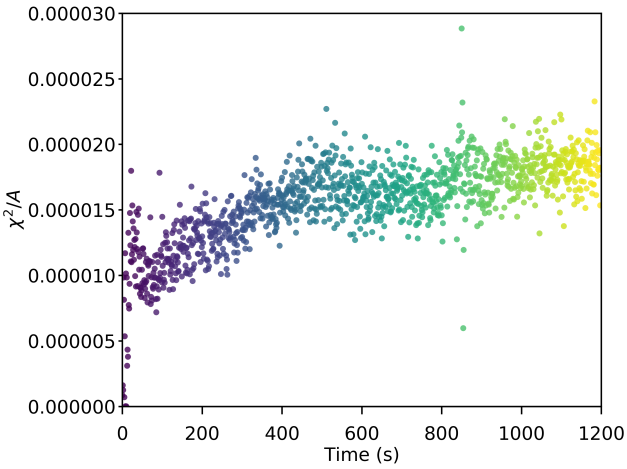

Figure S9. χ^2 normalised by the peak area as a function of time for the Gaussian fit.

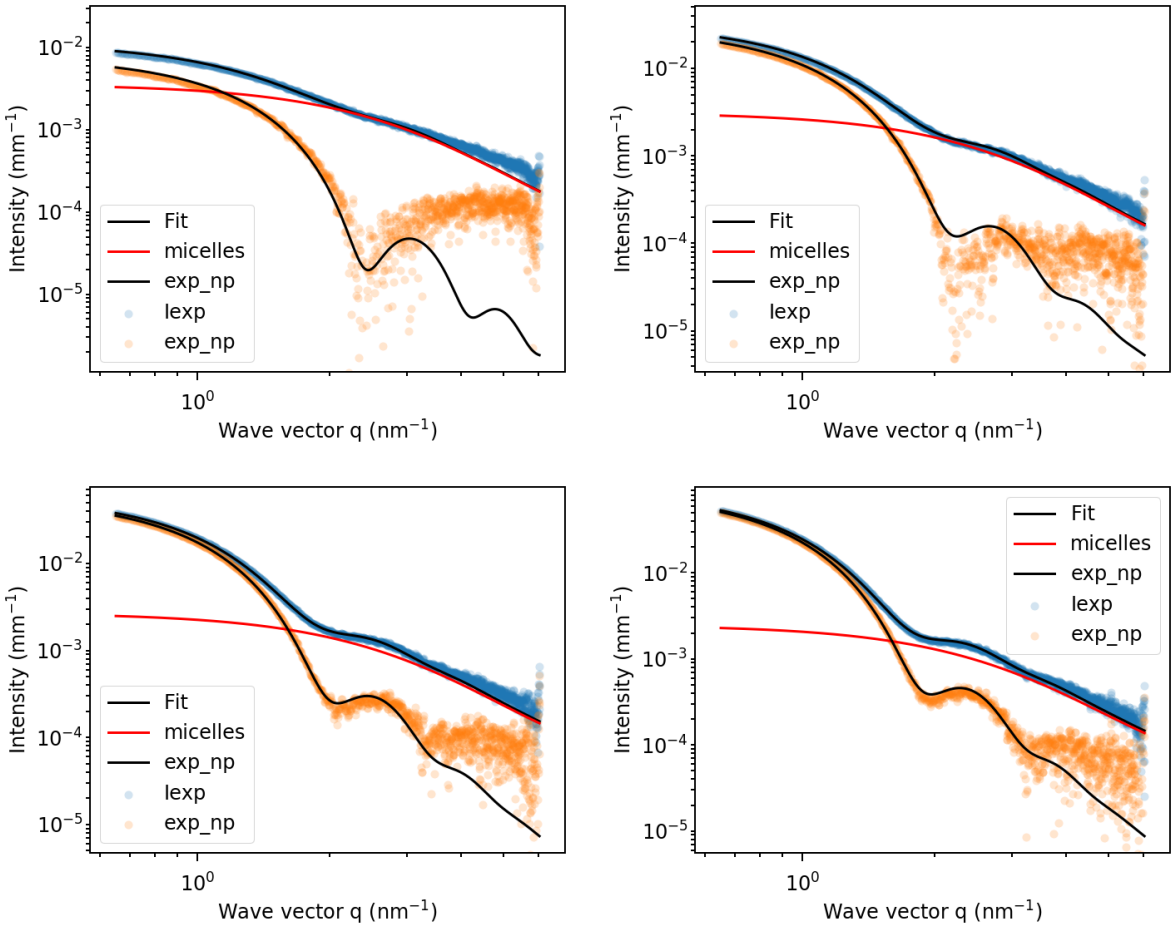

Figure S10. SAXS patterns and the fits with the different components of the intensity for early times. The total experimental intensity is in blue dots. The percursor micelles signal in the model is in red line and the orange dots correspond to the SAXS signal substracted from the micelles signal i.e. the first term in equation 1.

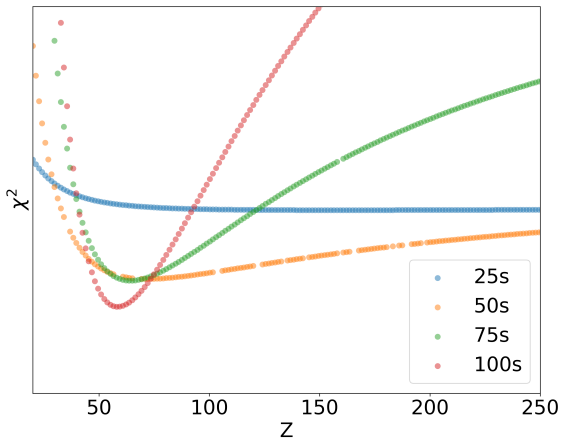

Figure S11. χ^2 parameter as a function of the polydispersity Z for different times during the formation of nanocrystals. The profile is almost flat at early times (see t=25s) but a clear minimum becomes visible as time advances.

We estimated that the fitting parameters can be determined with a high degree of accuracy after the 45 first seconds of the sequence in the case of the reference thiourea described in the main text. For earlier times, the signal corresponding to the nanoparticles is too small compared to the lead oleate micelles. The too low signal to noise ratio at high q during the first moments of the reaction prevents the reliable measurement of polydispersity. This parameter impacts the SAXS patterns at high q where oscillations appear. The amplitude of the oscillations are larger when polydispersity decreases. In the first moments of the reaction, the overall signal is dominated by the precursors and extracting the signal of the first nanoparticles at high q is not possible. This can is shown in a more quantitative fashion by examining the χ^2 values for fits performed with a fixed value of polydipsersity. At later times (figure S10) the signal to noise at high q is sufficient and the oscillation in intensity provides a very discriminating criteria for the fit. Hence the χ^2 vs time curve has a deep minimum which correspond to the best possible agreement between the model and the data. In constrast, at early times, χ^2 does not vary much over a large range of polydispersities showing that the data can not discriminate between different Z values. This impacts the correct measurements of the number of particles in solution even though $I(0)$ is measured with a high accuracy at all times because the number of particles depends on the polydiserpsity via equation 11 and $\langle V^2 \rangle$.

Another hypothesis which needs further discussion is the assumption that the nanoparticles are homogeneous spheres whose electron density does not change during the course of the reaction. The first assumption that could be questioned is the sphericity of the nanoparticles. Since the nanoparticles are crystalline, it is expected that they are faceted and thus that their real shape is polyhedral and not spherical. There are indeed multiple reports, both theoretical and experimental, that PbS nanocrystals are faceted. For example, it has been shown that PbS nanoparticles coud adopt octahedral or cuboctahedral shapes depending on their size[11]. To test if faceted nanoparticles would give different SAXS patterns, we simulated the scattered intensity for nanoparticles of different sizes from atomic models using CRYSOL[12]. Figure S12 shows the theoretical SAXS patterns calculated from the atomic coordinates of the model shown in the inset. We compared this patterns with the one of a sphere of the same volume. It is clear that the two patterns are not distinguishable. Thus, adopting an atomic model like the one presented here instead of an homogeneous sphere model will not change the outcome of the SAXS fitting.

This is in line with a theoretical report on the small angle scattering of polyhedral particles which showed that these are not discernable from the one of the isovolumetric sphere as soon as their sphericity is large enough[13]. There are significant differences in the case of a tetrahedron which has a low degree of sphericity (this can be quantified through the difference between the Guinier radius and the radius of the isovolumetric sphere). The fact that our PbS nanocrystals have a high degree of sphericity is supported by the perfect fits obtained by a spherical model. Had the particles been tetrahedral, a fit with a spherical model would have yield important discrepancies in a significant part of the wavevector range. We are thus confident that our hypothesis of high sphericity is solid.

We also may wonder if this assumption of sphericity does not impact in a quantitative fashion the concentration in particles or the polydispersity extracted from the fitted parameters. When we fit the patterns with a sphere model we find a set of parameters: mean radius, polydisersity. With another model we would have found another set of parameters. Since the concentration in particles depends on the size distribution via the intensity at $q \to 0$, it is thus legitimate to ask if the concentration in particles

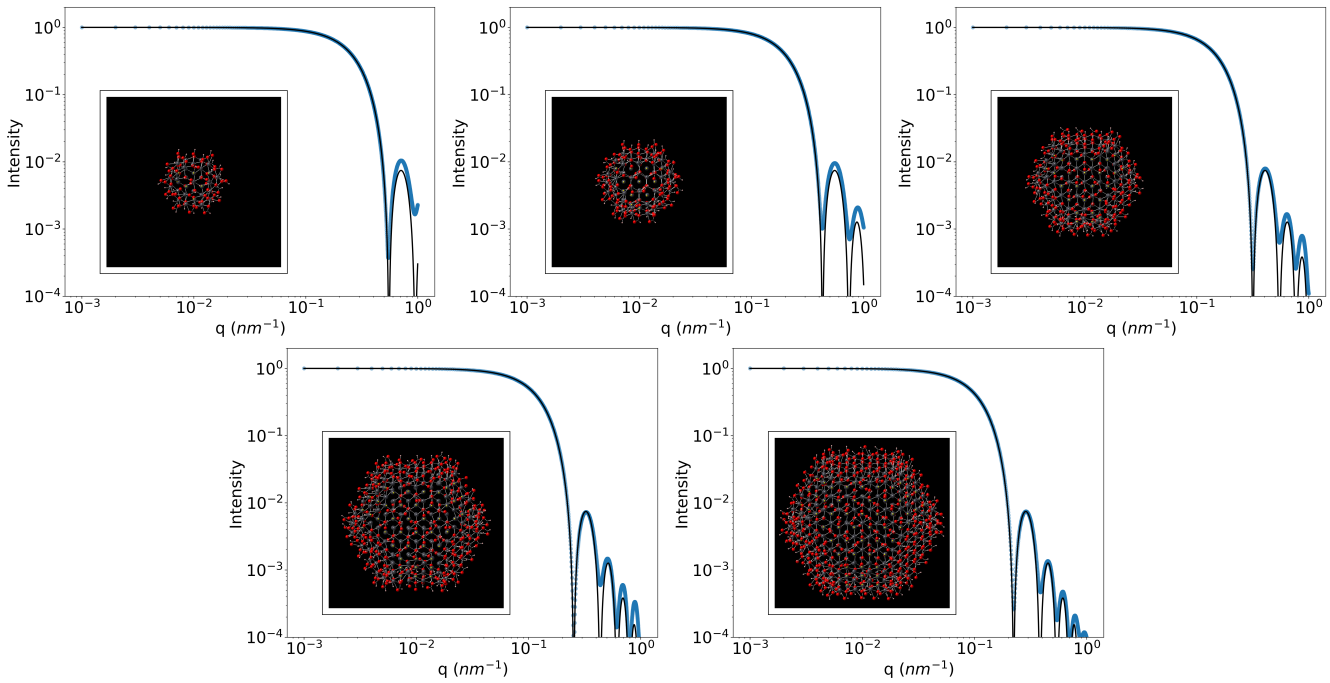

Figure S12. Simulated SAXS patterns for PbS nanoparticles with varying sizes from 1.6 to 4 nm in diameter. Blue points correspond to the SAXS intensity calculated with CRYSOL and the solid black lines are fits to a model of homogeneous shperes.

would be different with this other set of parameters.

In the monodisperse case, the concentration in particles is the same in the two cases because the two fits give the same intensity at every q, we have the same mean volume in the two cases. This was noted by Li et al.[13] who compared the SAXS patterns normalized by the radius of the isovolumetric sphere. Fundamentally, this comes from the fact that the volume the particles is linked to the invariant through $2\pi^2 I(0)/Q = V$ where $Q = \int I(q)q^2 dq$ is the invariant. This quantity only depends on the intensity and is model independant.[14] Thus, two particle models which yield the same SAXS pattern correspond to a unique particle volume. In the polydisperse case, the invariant is not directly proportional to the volume but to the ratio between the mean volume and the mean volume squared: $\frac{Q}{I(0)} = \frac{<V>}{<V^2>}$ and we must compare the mean volume squared in the case of a sphere and in the case of a polyhedra. Sphericity is likely to increase as the size increases and thus polydispersity will be less and less overestimated. If the number of particles is constant and the sphericity increases, that will be show up as a decrease in polydispersity in the fits and thus will artifactually induce an increase in the number of particles. However, since our model fits very well the data at high q, the Porod constant must be the same. This strongly bounds the range of polydisersity which are possible. In the case of polydisperse polyhedra, the Porod constant is the product of two terms $G \cdot P$ where G is a purely geometrical factor which only depends on the type of polyhedra and is given by: $G = \frac{2*\pi R_2 R_1^4}{R_3^4}$ where $R_1 = R_g/D$ and $R_3 = V/D^3$, while P is a polydispersity factor which depends solely on the width of the size distribution. For a Schultz distribution with parameter Z, it reads: $P = \frac{(Z+8)^2(Z+7)^2}{(Z+6)(Z+5)(Z+4)(Z+3)}$.

As a consequence, it may be difficult to disentangle polydispersity and shape since both factor are coupled. However, we can quantify to which extent one factor can compensate the other and assess if, in our case, a shape effect can have been misinterpreted as a polydispersity effect. Starting from the fact that the a model of polydisperse spheres fits our data at large wavevectors, we wondered if a model of polydisperse octahedron could also fit our data. If yes than we would have $(G \cdot P)_s = (G \cdot P)_o$ where the subscripts s and o refer to sphere and octahedron respectively. We know that $G_s/G_o = 0.735$ from the tabulated values given in[15], yielding $P_o = 0.735 P_s$. The polydispersties found for the spheres model correspond to Z values comprised between 40 and 100 and thus to P_s factors larger than 1.2. To compensate the polydispersity effect with a shape effect, we would thus need to have P_0 smaller than 0.93 which is impossible because the P(Z) function decreases monotically with Z and tends to 1 with Z. Thus with the small polydisersities found in our study, it is not possible to counfound the two factors.

Finally, we can question the assumption that the reaction occurs at constant contrast $\Delta\rho$. The variation in background scattering is taken into account through the addition of the term corresponding to the oleic acid micelles. The scattering length density of the nanoparticles is given by:

$$\sum_i \frac{bc_i}{V_m} = \rho_{N_a} \frac{\sum_i b_i}{\sum_i M_i} \tag{12}$$

where b is the electron scattering length, c_i is the concentration of the the different species and V_m the molecular volume. An easy calculation with the atomic molar mass and the number of electrons for Pb and S shows that a variation in the stoechiometry variation from PbS to Pb1.2S as described recently induces a variation of 0.05% of the scattering length density at constant density. The variation in density can be estimated from the measurement of the cell parameter by WAXS which changes by 0.07% yielding a variation in contrast of around 0.5%. Taken together, these variations are negligible compared to other experimental uncertainties.

3 Theory and simulation methods

We compare our experimental data to a theoretical model with population balance equations (PBE). The PBE predicts the evolution of the size distribution with time $n(r,t)$ and reads:

$$\frac{\partial n(r,t)}{\partial t} + \frac{\partial \left(G(r,t)n(r,t)\right)}{\partial r} = B(n,r,t) \tag{13}$$

where n is the number density of particles, r is the particle radius, t is the time and $G(r,t) = dr/dt$ is the growth rate of particles while the right hand term relates to the net creation of new particles which can occur *via* several different processes. Nucleation makes positive contributions to B while agglomeration makes negative contributions to B. In our model, we assume that only nucleation occurs and that nuclei are born with a negligible/undetectable size near $r = 0$. Therefore we can omit the source term $B(r,t)$ and instead impose a boundary condition $n(0,t)G(0,t) = J(t)$ where $J(t)$ is the nucleation rate at time t.

To focus our analysis on growth rate models, we solve the PBEs with experimentally measured inputs for other quantities. Specifically, the nucleation rate that appears in the boundary condition is obtained from the nanoparticle concentration vs. time curve as measured by SAXS (see Figure 4a of the main text). The nanoparticle concentration curve was fitted to a polynomial and then differentiated to obtain $J(t)$ (see Figure 4b in main text). We also used $C_{solute}(t)$ as determined from the NMR measurements (see Figure 3c in main text) which avoids the additional complications of a coupled species balance / population balance scheme.

We tested growth rate models of the form

$$G(r,t) = v_m k_G C_{solute}(t)/r^{\alpha} \tag{14}$$

where v_m is the molar volume of solid PbS, α sets the size dependence of the growth rate, $C_{solute}(t)$ is the dissolved PbS concentration, and k_G is a fit parameter. This growth rate expression can be used as an empiricism, with arbitrary values of α. This expression can also be derived from some mechanisms, giving specific interpretations and/or predictions for the values of k_G and α. The derivation typically begins with an equation $d[v_m^{-1}4\pi r^3/3] = 4\pi r^2[flux]$ where the flux expression may be from diffusion, from reactions per area per time, etc. One example of mechanistic model is diffusion controlled growth with a negligible solute concentration at saturation. This case gives $G = v_m D C_{solute}/r$, corresponding to the general growth rate expression with $\alpha = 1$ and $k_G = D$. Another example is reaction controlled growth with a first order dependence on concentration. As long as the surface reaction rates themselves do not depend on nanoparticle size, this case gives a size-independent growth rate law $G = v_m k_G C_{solute}$ where k_G an (apparent) rate constant for the first order rate constant. We also tested two models with no concentration dependence. These might arise if, for example, the nanoparticle surface is saturated throughout the growth process.

Each trial growth model was tested by solving the PBE equations (with $J(t)$ and $C_{solute}(t)$ inputs), using k_G as an adjustable parameter to match the observed average size vs. time curve as closely as possible. The polydispersity emerges as an unfitted prediction. The PBE yields the entire size distribution, but in this work we utilize only the mean radius and polydispersity because they are available from the experimental data.

3.1 Simulation methods

In this case, PBE has been solved numerically. Finite volume method based commercial solver FLUENT has been used to simulate the model. A unit volume of the well mixed reactor is considered. In a finite volume method, the unit volume is divided into a number of cells. In each cell, PBE (partial differential equation) is discretized in the following manner. First, the PBE has been discretized in the particle size domain using Hounslow method[16], which results in a set of ODEs with time derivatives. Then, these ODEs are discretized in a time domain using the implicit Crank-Nicolson method. This results in a set of algebraic equations, which have been solved by the iterative Gauss-Seidel method with successive under relaxation scheme and a relative tolerance of 10^{-6}. PBE module in the FLUENT successfully solves PBE. Nucleation and growth rates for the particles have been included in the module as user defined functions (UDF) written in C++. Nucleation rate is used as a boundary condition. Time step size and bins size are varied based on the growth rates. At the end, we get the number density distribution as output, from which we calculate the arithmetic mean radius (D10) and % polydispersity. Polydispersity is calculated as the ratio of standard deviation to the mean radius multiplied by 100.

3.2 Testing of different growth law

We initially examined three growth mechanisms. We first started with a surface reaction limited attachment growth law. Here, the growth rate depends on the solute concentration and not on the size of the particles ($\alpha = 0$). The corresponding growth rate expression is:

$$G = \frac{dr}{dt} = k_G \times C_{\text{solute}} \tag{15}$$

where k_G is the rate constant and C_{solute} is the PbS concentration.

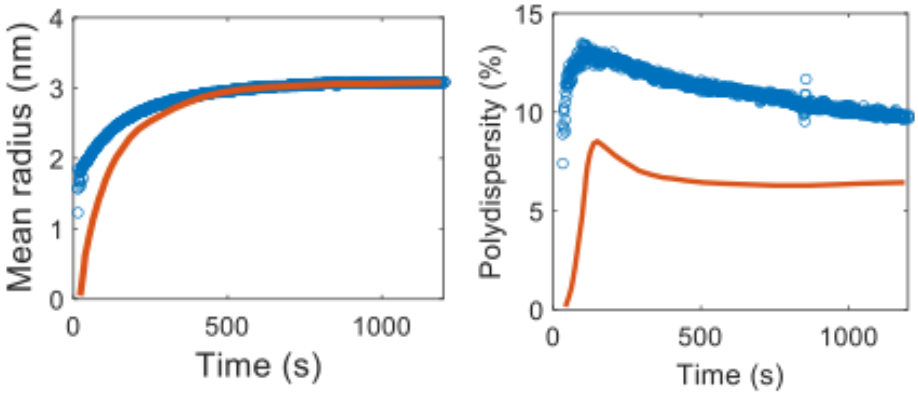

Figure S13. Evolution of mean size (left) and polydispersity (right) with concentration dependent growth $G = k_G C_{\text{solute}}$

Fig. S13 shows that this model cannot capture the experimental variation in either mean size or polydispersity. Though there is a match with the experimental size data at long times, the predictions are not satisfactory at short times and the polydispersity is poorly predicted at all times.

A second model assumes that particles grows by attachment at a constant frequency, independent of both particle size and the bulk PbS concentration i.e $G = k_G$. The model assumes that all parts of the surface are equally reactive and saturated with adsorbed PbS so that the rate does not depend on bulk PbS concentration. Fig.S14 shows that this model cannot predict the experimental variation in size vs. time.

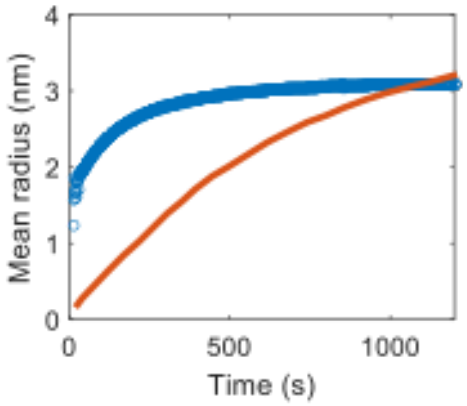

Figure S14. Measured (blue) and evolution of the mean radius vs. time with predictions (red) from a model with a constant growth rate which does not depend on particle size: $G = k_G$

A third model assumes that all the particles grow by the same number of molecules per unit time. If each particle grows with m molecules per second, the corresponding growth law can be expressed as:

$$G = \frac{dr}{dt} = \frac{m v_{molecular}}{4\pi r^2} \tag{16}$$

where $V_{molecular}$ is the molecular volume. Simulation results for this model are shown on figure S15. According to this model, particles stop growing because of the size dependence (r^{-2}) in the growth law and not because of a dropping solute concentration. However, predictions from this model for the mean size are as high as 40%, and the polydispersity predictions clearly deviate from that observed in the experiments.

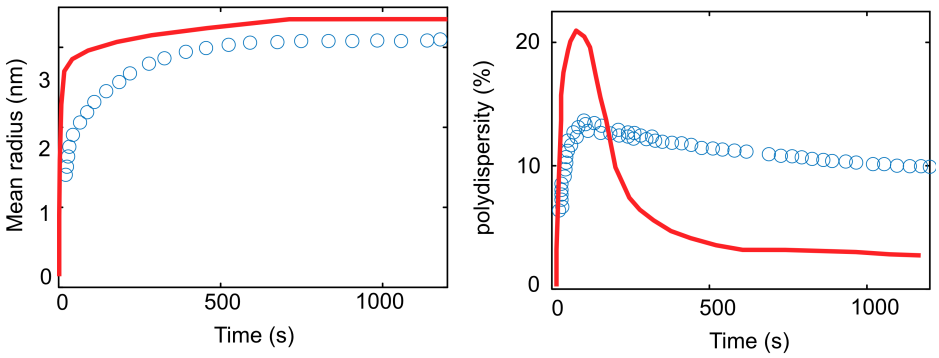

Figure S15. Evolution of mean size (left) and polydispersity (right), for a fitted value of $m = 6.7$ molecules per particle per second. In this case, growth continues as long as 6.7 molecules per particle per second are available for the growth of all particles.

We now consider a family of growth models that include both size and concentration dependence of the form

$$G = \frac{dr}{dt} = \frac{v_m k_G C_{solute}}{r^{\alpha}} \tag{17}$$

Here k_G is the fitting constant and α as the exponent. This model can accurately predict the mean radius and polydispersity data for $\alpha = 1$ (figure S16.A and B). We also tested other values of α. In particular, the model with $\alpha = 1.5$ yields excellent results. We ultimately focus on results from the $\alpha = 1$ case because (unlike the $\alpha = 1.5$ case) it points to mechanistic interpretations like diffusion control.

3.3 Mass balance check

For all models, we carried out a mass balance check by comparing the predicted mass of solid PbS to the experimentally measured solid PbS content. In figure S17, we show mass balance check for 4Cl-Ph-DD-TU as an example for the diffusion controlled growth laws, i.e. $G = v_m D C_{solute}/r$. The model which accurately describes the growth kinetics (eq. 17) maintains the accurate mass balance. Models that do not accurately describe the mean size and polydispersity also produce large mass balance errors.

3.4 Derivation of growth model in the presence of ligand shell

In order to investigate this in depth, we began from a model including all resistances: (1) an inner ligand shell surrounding the nanoparticle, (2) an outer boundary layer for diffusion to the nanoparticle surface, and (3) a surface reaction at the nanoparticle surface. Here we outline the derivation for the overall growth rate law including all three resistances. The procedure for these derivations can be found in the chemical engineering literature, e.g. in[17] C_{solute}, $C_{(R+\ell)^+}$, $C_{(R+\ell)^-}$ and C_R designate PbS concentrations respectively in the bulk, just outside the solvent - ligand shell interface, just inside the solvent - ligand shell interface, and at the nanoparticle - ligand shell interface. ℓ is the thickness of the ligand shell. We use D_{shell} for the diffusivity of PbS inside the ligand shell, D_{bulk} for the diffusivity of PbS in solution, K for the partition coefficient of PbS from the solution to the ligand shell region, and k for the attachment reaction at the nanoparticle surface.

Steady-state expressions for the attachment rate are given as follows at three different locations. At the surface ($r = R$):

$$N = kC_R 4\pi R^2 \tag{18}$$

For $R < r < R + \ell$:

$$N = 4\pi r^2 D_{shell} dC/dr \tag{19}$$

For $r > R + \ell$:

$$N = 4\pi r^2 D_{bulk} dC/dr \tag{20}$$

And the concentrations $C_{(R+\ell)^+}$ and $C_{(R+\ell)^-}$ are related by a partition coefficient:

$$K = C_{(R+\ell)^+}/C_{(R+\ell)^-} \tag{21}$$

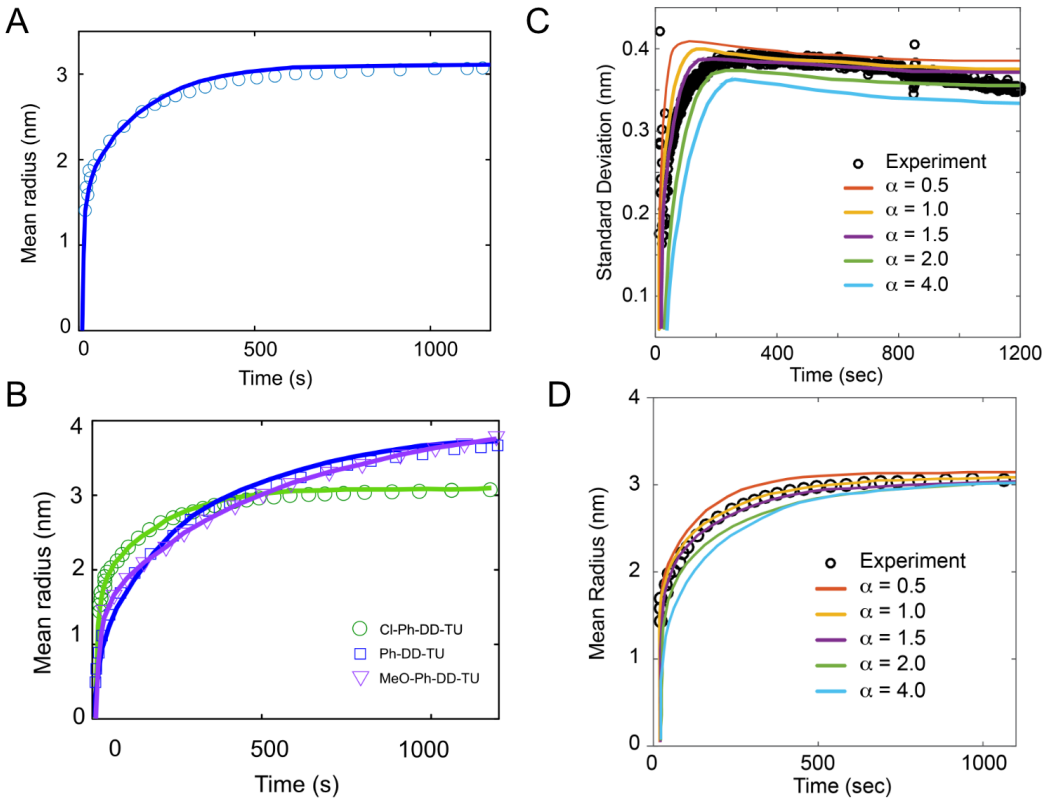

Figure S16. Comparison of simulation results from models with different order of size dependence $G = \frac{v_m k_G C_{solute}}{r^{\alpha}}$: $\alpha = 1$ for mean radius and Cl-Ph-DD thiourea (A) and different thioureas (B), α varying from 0.5 to 4 for standard deviation and radius evolution for the Cl-Ph-DD thiourea (C,D).

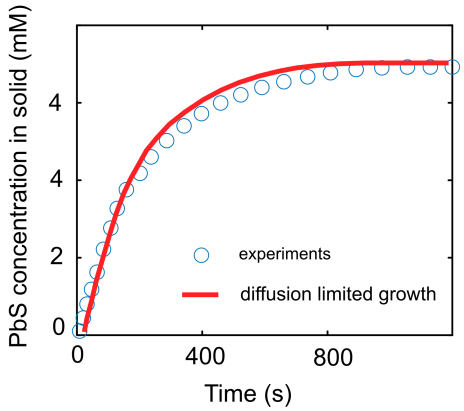

Figure S17. Comparison of PbS concentrations in solid from simulation and experiment. Simulation with growth law given in eq. 17 with $\alpha = 1$

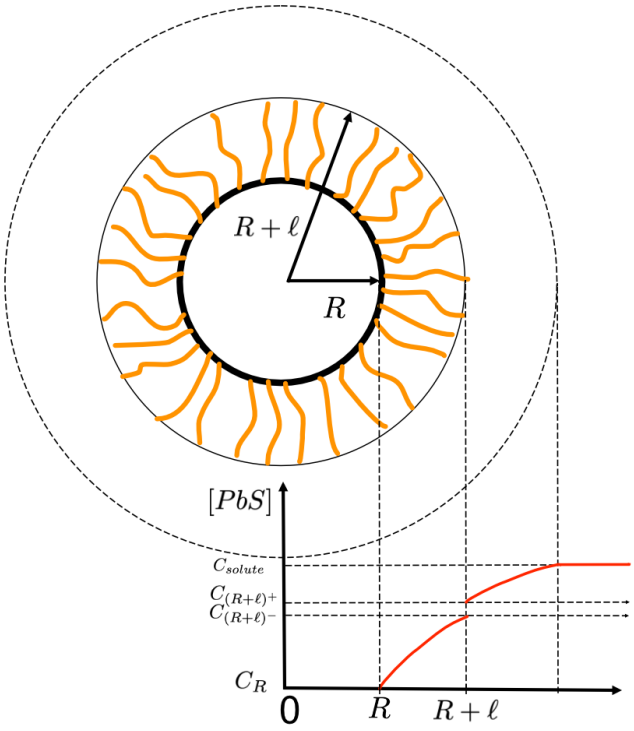

Figure S18. Resistances to PbS attachment include diffusion to the ligand shell, diffusion through the ligand shell, and reaction at the nanoparticle surface.

Integrating the differential expressions gives equations for the attachment rate N in terms of boundary concentrations. Specifically, $4\pi D_{shell}(C_{(R+\ell)^-} - C_R) = N(1/R - 1/(R+\ell))$ and $4\pi D_{bulk}(C_{solute} - C_{(R+\ell)^+}) = N/(R+\ell)$. When combined with the surface reaction rate expression $N = kC_R 4\pi R^2$, these give four equations and four unknowns to identify the attachment rate N and the three interfacial concentrations C_R, $C_{(R+\ell)^-}$, and $C_{(R+\ell)^+}$. The resulting expression for N has three terms corresponding to bulk diffusion, ligand shell diffusion, and surface reaction resistances.

Using $N = 4\pi R^2 v_m^{-1} dR/dt$ and $G = dR/dt$ gives an expression for the growth rate:

$$G = \frac{v_m C_{solute}}{\frac{1}{kK} + \frac{R^2}{(R+\ell)D_{bulk}} + \frac{R\ell}{D_{shell}K(R+\ell)}} \tag{22}$$

The terms in the denominator are resistances due to the surface reaction, the bulk diffusion, and the ligand shell penetration, respectively. In principle, all of these terms can be computed using molecular simulations and/or electronic structure calculations, providing a link to future computational work. Note that D_{bulk} is denoted D_{solute} in the main text. Also note that the equation $N = 4\pi R^2 v_m^{-1} dR/dt$ ignores moving boundary effects which dramatically complicate the analysis, but lead to small corrections when $v_m << C_{solute}^{-1}$.

If ligand shell penetration is the dominant resistance, then the growth rate expression simplifies to

$$G = \frac{v_m C_{solute} D_{shell} K(R+\ell)}{R\ell} \tag{23}$$

The parameters D_{shell} and K are both unknown, but they appear as a single lumped product. In the calculations, we have used the value $\ell = 2$ nm. Figure 5 of the main text shows that mean radius and polydispersity calculated from this model matches experimental data well with a consistent fitted value of $D_{shell}K$ across all three thiourea precursors. This indicates that the size focusing behavior in our experiments can be explained by the rate for solute penetration of the ligand shell, which the model suggests will become more difficult as particles become larger. The result also suggests that the unexpectedly small PbS diffusivity and accurate mean size and polydispersity predictions from the diffusion control model were probably fortuitous fits. The ligand-shell penetration models and bulk diffusion control models have similar size-dependences for small nanoparticles.

Thus the diffusion control model was inadvertently capturing the size dependence due to a ligand shell penetration resistance, or perhaps due to some other size-dependent rate process in the attachment pathway.

3.5 Effect of nucleus size on the final particle size

To ensure that our results were not affected by assuming nuclei have size zero, we also carried out simulations with nuclei "born" at different sizes. The results are shown in figure S19. The results show that the time for nuclei to grow from critical size to observable sizes is essentially the same, whether they start from zero, ten, or even 100 PbS units. By comparision the final particle sizes include thousands of PbS units. Predictions at later times are also unaffected by the assumed critical size.

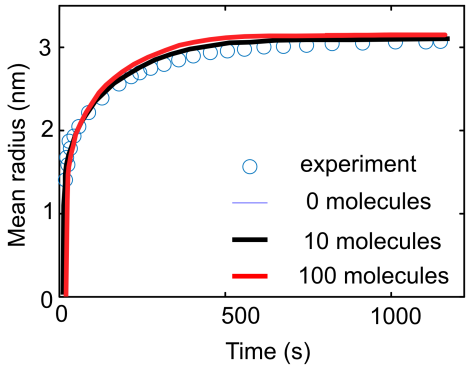

Figure S19. Comparison of simulation results from models with different order of size dependence.

3.6 Diffusivity measurements and viscosity effects

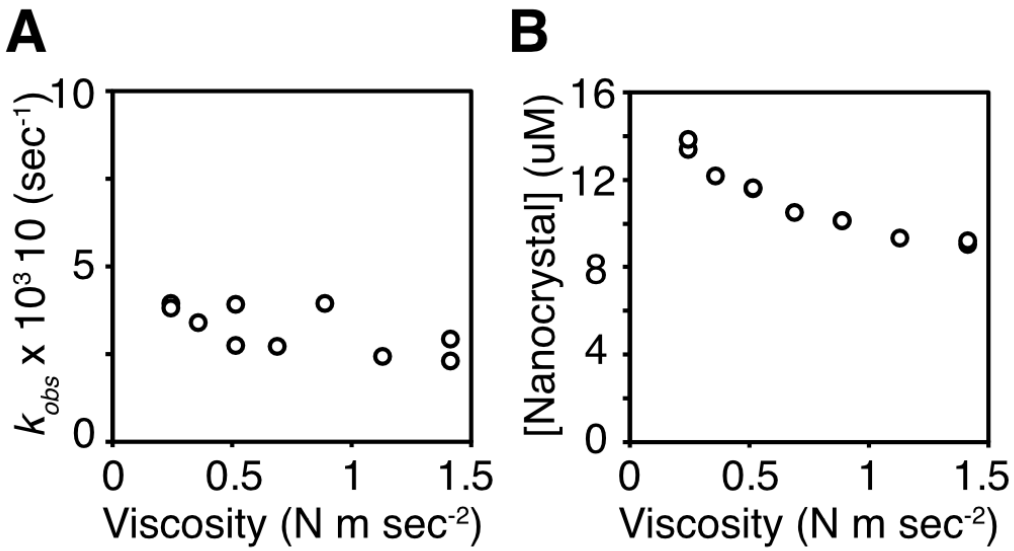

Figure S20. Variation of the reaction constant and nanocrsytal concentrations at the end of the reaction for different solvent viscosities.

PbS syntheses were conducted in several alkane solvents ranging from C8 to C20 (octane, decane, dodecane, tetradecane, hexadecane, octadecane, and eicosane). The viscosity of these solvents varies from 0.24 to 1.41 N m sec^{-2} at the reaction temperature (100 °C).[18] Diffusion is inversely related to viscosity of the solvent through the Stokes-Einstein relation. Thus, we are able to systematically adjust the diffusivity of reaction components and study its effect on the synthesis. N-phenyl-N'-n-dodecylthiourea is reacted with lead oleate at 100 °C and the size and concentration of PbS monitored throughout the reaction via aliquots. Fig. S20.A. shows the observed reaction rates as a function of solvent viscosity. The precursor reactivity is not significantly influenced by the viscosity change. The final concentration and size of nanocrystals is weakly dependent

on the viscosity as shown in Fig. S20.B. Increasing viscosity results in fewer, larger nanocrystals, a trend that is contrary to a diffusion-limited growth model, where reducing the solute diffusivity would reduce the growth rate and result in a higher concentration of smaller nanocrystals.

Experiments were carried out using the workstation for automated nanomaterial design and analysis at the Molecular Foundry, Lawrence Berkeley National Laboratory. All manipulations and reactions were conducted in a nitrogen-filled glovebox. Reactions were prepared by adding 9.5 mL of the desired alkane solvent and 0.24 mmol (184.8 mg, 1.2 eq.) of lead oleate to a 40 mL reaction vial. Two rare-earth magnetic stir bars were added to each vial. Separately, a stock solution of N-(4-methoxyphenyl)-N'-n-dodecylthiourea in diphenyl ether was prepared by dissolving 2 mmol (701 mg) in 5 mL (5.365 g) diphenyl ether in a vial fitted with a stir bar. The vials are heated to 100 °C before whereupon the thiourea stock solution (0.5 mL) is injected into the lead oleate solution. Aliquots are taken over 84 minutes of total reaction time that were diluted with tetrachloroethylene for UV-Vis and UV-Vis-NIR absorbance spectroscopy analysis. The sample were exposed to air briefly prior to the absorbance spectroscopy.

4 Supplementary figures

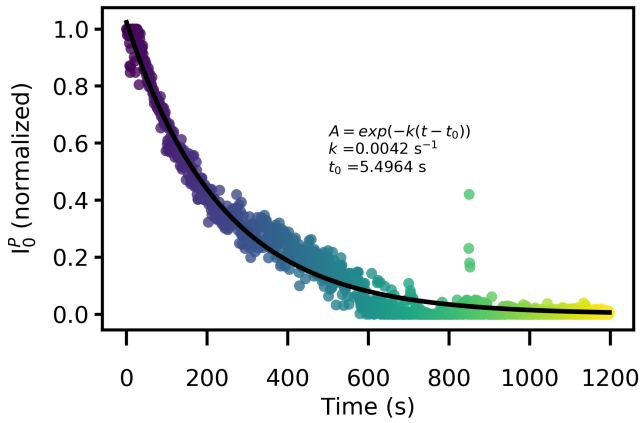

Figure S21. Evolution of the I_0^P parameter normalized to the first value of the time series as a function of time. This quantifies concentration in lead oleate precursor in solution.

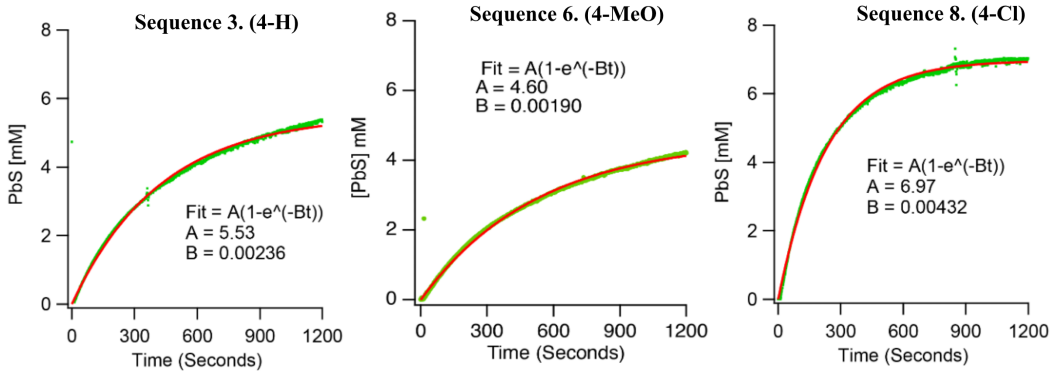

Figure S22. Concentration in PbS within the nanoparticles as measured by SAXS for 3 different precursors. The kinetics are fitted to a first order law whose constants are shown.

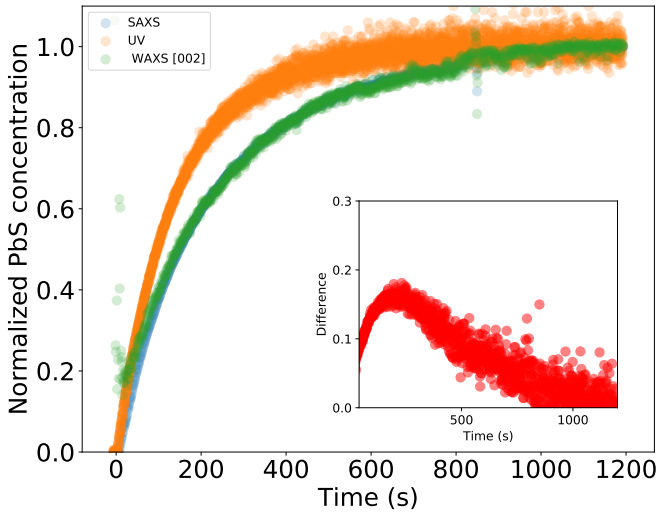

Figure S23. Kinetics of the PbS concentration as probed by UV VIS, SAXS and the [002] peak in WAXS for the N-4-chloro-phenyl-N'-dodecylthiourea.

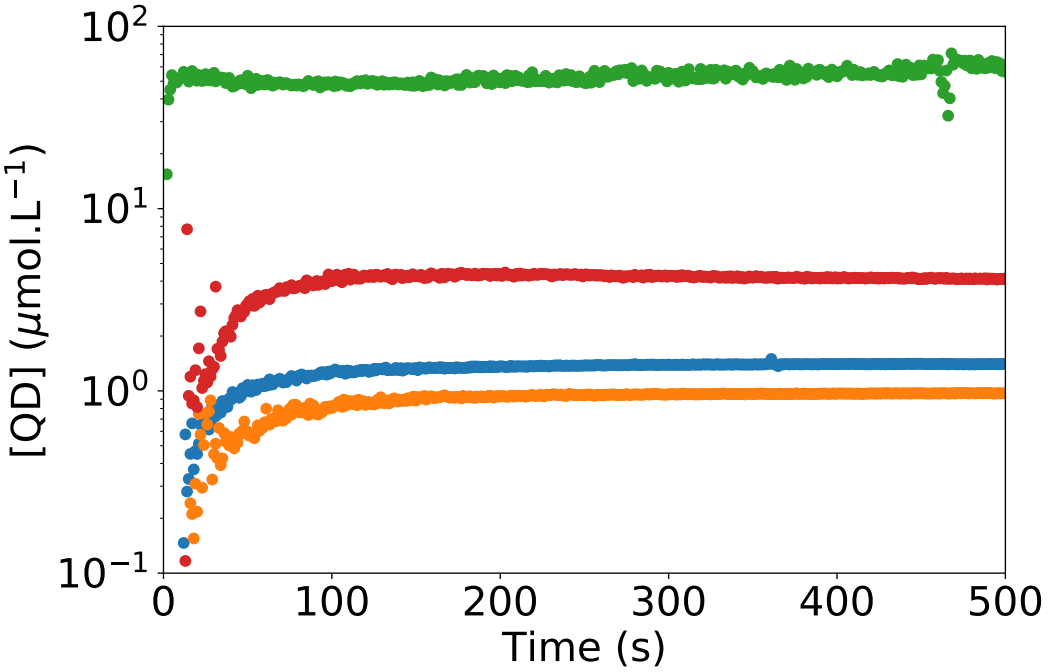

Figure S24. Evolution of the nanocrystal concentration with time for 4 different thioureas. The red, blue and orange traces correspond to the TU displayed in figure 4a of the main text. The green points correspond to 3-5-2-iPr-Ph-TU.

References

1. Hendricks, M. P., Campos, M. P., Cleveland, G. T., Plante, I. J.-L. & Owen, J. S. A tunable library of substituted thiourea precursors to metal sulfide nanocrystals. *Science* **348**, 1226–1230, DOI: 10.1126/science.aaa2951 (2015).
2. Wong, R. & Dolman, S. J. Isothiocyanates from Tosyl Chloride Mediated Decomposition of in Situ Generated Dithiocarbamic Acid Salts. *J. Org. Chem* **72**, 3969–3971, DOI: 10.1021/jo070246n (2007).
3. Ramadas, K., Srinivasan, N. & Janarthanan, N. A facile conversion of symmetrical to unsymmetrical thioureas. *Tetrahedron Lett.* **34**, 6447–6450, DOI: 10.1016/0040-4039(93)85067-7 (1993).
4. Narayanan, T. *et al.* A multipurpose instrument for time-resolved ultra-small-angle and coherent X-ray scattering. *J. Appl. Crystallogr.* **51**, 1511–1524, DOI: 10.1107/S1600576718012748 (2018).
5. Pérez, F. & Granger, B. IPython: A System for Interactive Scientific Computing. *Comput. Sci. Eng.* **9**, 21–29, DOI: 10.1109/MCSE.2007.53 (2007).
6. ABECASSIS, B., CASTRO, N., GRILLO, I. & JANA, S. Structure of ligand self-assembled monolayers at the surface of quantum dots and Nanoplatelets in solution, DOI: 10.5291/ILL-DATA.9-12-464 (2016). Type: dataset.
7. Maes, J. *et al.* Size and Concentration Determination of Colloidal Nanocrystals by Small-Angle X-ray Scattering. *Chem. Mater.* **30**, 3952–3962, DOI: 10.1021/acs.chemmater.8b00903 (2018).
8. Kotlarchyk, M. & Chen, S.-H. Analysis of small angle neutron scattering spectra from polydisperse interacting colloids. *The J. Chem. Phys.* **79**, 2461, DOI: 10.1063/1.446055 (1983).
9. Aragón, S. R. Theory of dynamic light scattering from polydisperse systems. *The J. Chem. Phys.* **64**, 2395, DOI: 10.1063/1.432528 (1976).
10. Patterson, A. L. The Scherrer Formula for X-Ray Particle Size Determination. *Phys. Rev.* **56**, 978–982, DOI: 10.1103/PhysRev.56.978 (1939).
11. Choi, H., Ko, J.-H., Kim, Y.-H. & Jeong, S. Steric-Hindrance-Driven Shape Transition in PbS Quantum Dots: Understanding Size-Dependent Stability. *J. Am. Chem. Soc.* **135**, 5278–5281, DOI: 10.1021/ja400948t (2013).
12. Svergun, D., Barberato, C. & Koch, M. H. J. *CRYSOL* – a Program to Evaluate X-ray Solution Scattering of Biological Macromolecules from Atomic Coordinates. *J. Appl. Crystallogr.* **28**, 768–773, DOI: 10.1107/S0021889895007047 (1995).
13. Li, X. *et al.* Scattering functions of Platonic solids. *J. Appl. Crystallogr.* **44**, 545–557, DOI: 10.1107/S0021889811011691 (2011).
14. Porod, G. General Theory. In *Small Angle X-Ray Scattering*, 17–51 (Academic Press Inc, London ; New York, 1982).
15. Senesi, A. & Lee, B. Scattering functions of polyhedra. *J. Appl. Crystallogr.* **48**, 565–577, DOI: 10.1107/S1600576715002964 (2015).
16. Hounslow, M. J., Ryall, R. L. & Marshall, V. R. A discretized population balance for nucleation, growth, and aggregation. *AIChE J.* **34**, 1821–1832, DOI: https://doi.org/10.1002/aic.690341108 (1988).
17. Bird, R. B., Stewart, W. E. & Lightfoot, E. N. *Transport Phenomena* (John Wiley & Sons, New York, 2007), revised second edn.
18. Viswanath, D. S., Ghosh, T., Prasad, D. H. L., Dutt, N. V. K. & Rani, K. Y. *Viscosity of Liquids: Theory, Estimation, Experiment, and Data* (Springer Netherlands, 2007).